the plant journal

SEB SOCIETY FOR EXPERIMENTAL BIOLOGY

The Plant Journal (2023) **116,** 855–870 doi: 10.1111/tpj.16414

Cellulose assembles into helical bundles of uniform handedness in cell walls with abnormal pectin composition

Adam M. Saffer[1,*], Tobias I. Baskin[2], Amitabh Verma[3], Thomas Stanislas[4], Rudolf Oldenbourg[3] and Vivian F. Irish[1,5,*]

[1]*Department of Molecular, Cellular and Developmental Biology, Yale University, New Haven, Connecticut 06520, USA,*

[2]*Biology Department, University of Massachusetts, 611 N. Pleasant St, Amherst, Massachusetts 01003, USA,*

[3]*Marine Biological Laboratories, 7 MBL Street, Woods Hole, Massachusetts 02543, USA,*

[4]*Laboratoire de Reproduction et Développement des Plantes, Université de Lyon, ENS de Lyon, UCBL, INRAE, CNRS, 46 Allée d'Italie, 69364 Lyon Cedex 07, France, and*

[5]*Department of Ecology and Evolutionary Biology, Yale University, New Haven, Connecticut 06520, USA*

Received 27 October 2022; accepted 19 July 2023; published online 7 August 2023.
*For correspondence (e-mail adam.saffer@yale.edu; vivian.irish@yale.edu)

SUMMARY

Plant cells and organs grow into a remarkable diversity of shapes, as directed by cell walls composed primarily of polysaccharides such as cellulose and multiple structurally distinct pectins. The properties of the cell wall that allow for precise control of morphogenesis are distinct from those of the individual polysaccharide components. For example, cellulose, the primary determinant of cell morphology, is a chiral macromolecule that can self-assemble *in vitro* into larger-scale structures of consistent chirality, and yet most plant cells do not display consistent chirality in their growth. One interesting exception is the *Arabidopsis thaliana rhm1* mutant, which has decreased levels of the pectin rhamnogalacturonan-I and causes conical petal epidermal cells to grow with a left-handed helical twist. Here, we show that in *rhm1* the cellulose is bundled into large macrofibrils, unlike the evenly distributed microfibrils of the wild type. This cellulose bundling becomes increasingly severe over time, consistent with cellulose being synthesized normally and then self-associating into macrofibrils. We also show that in the wild type, cellulose is oriented transversely, whereas in *rhm1* mutants, the cellulose forms right-handed helices that can account for the helical morphology of the petal cells. Our results indicate that when the composition of pectin is altered, cellulose can form cellular-scale chiral structures *in vivo*, analogous to the helicoids formed *in vitro* by cellulose nano-crystals. We propose that an important emergent property of the interplay between rhamnogalacturonan-I and cellulose is to permit the assembly of nonbundled cellulose structures, providing plants flexibility to orient cellulose and direct morphogenesis.

Keywords: Cell wall, cellulose, chirality, helical growth, pectin.

INTRODUCTION

Plant cells are surrounded by cell walls composed predominantly of polysaccharides, including cellulose, hemicelluloses, and pectins, that determine cell morphology (Cosgrove, 2018). The chemical and mechanical properties of cell walls are significantly different from their constituent components, and we are only just beginning to understand how the emergent properties of cell walls arise from the interplay between cell wall components. For example, the chiral molecule cellulose provides the predominant contribution to the mechanical properties of the cell wall (Zhang et al., 2021); and yet, cells and organs only occasionally grow with a visible helical twist, indicating that the chirality of cellulose is typically not manifested in the overall mechanics of the cell wall when cellulose interacts with other polymers. It is unclear how chirality can be transmitted across length scales from molecules to cells, or how the relationships between different polysaccharides might prevent the emergence of chirality on the length scale of a cell.

While many aspects of the macromolecular structures of cell wall components and their interactions are yet to be elucidated, the primary structures of most polysaccharides are generally well understood. Cellulose is organized into long partially crystalline microfibrils containing 18 to 24 chains of (1,4)-β-D-linked glucans (Polko & Kieber, 2019). Microfibrils are typically well aligned within each layer of the cell wall, making cellulose the major determinant of mechanical anisotropy, with maximal cell expansion rate

typically perpendicular to the orientation of the microfibrils (Baskin, 2005). Cellulose is embedded within a matrix of hemicellulose and pectin. The pectins comprise several structurally distinct polysaccharides that have numerous covalent and noncovalent interactions with each other and with other cell wall components (Saffer, 2018). The most abundant pectin is typically homogalacturonan, a polymer of galacturonic acid (Atmodjo et al., 2013). Homogalacturonan can be decorated with sidechains to make other pectins such as rhamnogalacturonan-II (RG-II) (Ndeh et al., 2017; Pabst et al., 2013). The pectin rhamnogalacturonan-I (RG-I) has a distinct structure with a repeating rhamnose-galacturonic acid backbone, and many of the rhamnose residues carry neutral sugar sidechains including arabinans and galactans (Atmodjo et al., 2013). Pectins are important for cell–cell adhesion (Daher & Braybrook, 2015), tensile strength (Ryden et al., 2003), and influencing cell expansion (Saffer, 2018), although the functions of some pectins are still unclear (Ebert et al., 2018; Jensen et al., 2008). Pectins can also interact with cellulose (Dick-Perez et al., 2011; Lin et al., 2016; Wang et al., 2012, 2015; Zykwinska et al., 2005, 2007) and influence cellulose architecture (Du et al., 2020; Thimm et al., 2009; Yoneda et al., 2010).

One system that is well suited for studying the contributions of cell wall components to cellular morphology is conical petal epidermal cells. Petals in most angiosperms have conically shaped epidermal cells (Kay et al., 1981) that are an adaptive trait for attracting pollinators (Whitney et al., 2011). The upper conical portion of the cell protrudes from the plane of the organ and has minimal direct physical interaction with neighboring cells, simplifying the observation and interpretation of cell morphology mutants; the lower portion of the cell contacts adjacent cells to potentially contribute to overall petal morphology. *Arabidopsis thaliana* petals are relatively simple organs with mesophyll surrounded by a layer of epidermal cells. Epidermal cells in the basal claw region are longitudinally elongated, while epidermal cells in the distal blade are slightly domed on the abaxial side and have a distinctive conical shape on the adaxial side (Irish, 2008). Conical petal epidermal cells have been used as an assay system in genetic screens to identify multiple mutations that alter cell morphology (Ren et al., 2017; Saffer & Irish, 2017; Yang et al., 2019).

One such screen identified a mutation in the gene *RHAMNOSE BIOSYNTHESIS1* (*RHM1*) that results in a helical morphology of the conical petal epidermal cells. In *rhm1* mutants, the conical petal cells twist into left-handed helices, and at the organ level, petals as well as roots display left-handed growth (Saffer et al., 2017). The *rhm1-1* nonsense allele causes slight defects in cell expansion, whereas the more phenotypically severe *rhm1-3* allele with a missense mutation in the dehydratase domain causes a more substantial decrease in cell expansion (Saffer et al., 2017). *RHM1* encodes one of the three *Arabidopsis thaliana* rhamnose synthases, which catalyze the production of UDP-L-rhamnose (Diet et al., 2006; Oka et al., 2007; Reiter & Vanzin, 2001), the donor for the transfer of rhamnose to the backbone of RG-I and to the sidechains of RG-II. Petals from the different *rhm1* alleles have between approximately 20 and 55% lower levels of RG-I backbone compared with the wild type; genetic experiments are consistent with the helical growth of *rhm1* mutant petals resulting from these reduced levels of RG-I (Saffer et al., 2017; Saffer & Irish, 2018).

Helical growth in plant organs can be caused by various mutations or chemical inhibitors, most of which result in cortical microtubules in growing cells becoming organized helically with a uniform handedness (Smyth, 2016), unlike typical growing cells where cortical microtubules are transverse to the axis of greatest expansion rate (Liang et al., 1996). Cortical microtubules direct the deposition of cellulose microfibrils (Baskin, 2001), although cellulose synthases can also sometimes track existing cellulose microfibrils (Chan & Coen, 2020), and there are instances where the microtubules and cellulose microfibrils are not co-aligned (Emons et al., 1992). Therefore, helical microtubule arrays typically result in helically arranged cellulose of the same handedness. Strikingly, the helical growth of *rhm1* roots is independent of microtubules (Saffer et al., 2017).

Cellulose is the primary determinant of the mechanical axes of the plant cell and, therefore, of the direction of anisotropic cell expansion (Baskin, 2005). When cellulose becomes organized helically around a cell, there is then a mismatch between the geometric and mechanical axes of the cell. Theoretical and modeling approaches indicate that such a mismatch should cause cellular twisting to robustly emerge with opposite handedness to the helical cellulose orientation (Chakraborty et al., 2021; Probine, 1963; Sellen, 1983; Wada & Matsumoto, 2018). These theoretical predictions are supported by observations of various cell types growing helically in a handedness that is the opposite of their helically arranged microfibrils (Roelofsen, 1966) or helically arranged microtubules (Ishida et al., 2007). The mechanical coupling that results from cell–cell adhesion and the spatial constraints on plant cell growth then leads to the helical growth of cells being transmitted to the scale of organs (Verger et al., 2019).

Based on this framework, we suggest that decreased RG-I synthesis alters the emergent architectural properties of the cell wall, amplifying an innate chirality of a macromolecule other than microtubules. Because cellulose is a major structural component of plant cells and microfibrils have uniform chirality (Hanley et al., 1997; Usov et al., 2015), we hypothesized that the helical growth of *rhm1* involves changes to cellulose organization. We report here that in *rhm1* petals cellulose aberrantly bundles and becomes organized into right-handed helices, indicating a

rhamnose-containing cell wall polysaccharide prevents cellulose from assembling into a mesoscale chiral structure.

RESULTS

Mutations in *RHM1* cause cellulose bundling

To investigate cellulose organization, we used field-emission scanning electron microscopy (FESEM) to image the innermost cell wall of *Arabidopsis thaliana* adaxial petal epidermal cells that had been cut open (Figure 1a). Images of the cut edges revealed thin cell walls, less than 100 nm thick, overlaid with a thick cuticle that folds outward to create cuticular ridges (Figure 1b). The cell wall is indented underneath the cuticular ridges, appearing slightly darker in the FESEM images (Figure 1b,c).

Wild-type conical epidermal petal cell walls had transversely oriented fibers, forming hoops around the conical portion of the cells (Figure 1c). Among all wild-type cells examined, cell wall organization was substantially similar. The fibers in the wild-type cell walls were relatively homogeneous in size, with an average width of approximately 11 nm (Figure 1c,j). For land plants, individual cellulose microfibrils are thought to be approximately 3 nm in diameter (Rongpipi et al., 2018); therefore, the fibers we observed are plausibly each a single elementary cellulose microfibril sheathed in a layer of matrix polysaccharides and covered by the roughly 2 nm of platinum deposited during sample preparation. Hereafter, we refer to these less than 20 nm wide fibers as microfibrils, although some might contain more than one elementary cellulose microfibril.

Conical petal epidermal cells in plants homozygous for *rhm1* alleles had a range of cellulose-organization phenotypes. In *rhm1-1*, most cells were indistinguishable from those of the wild-type, but some mutant cells had irregular arrangements of cellulose, including microfibrils running roughly parallel to the cuticular ridges (Figure 1d) or less uniformly oriented. In *rhm1-3*, we observed a more severe disruption of cellulose architecture, as many cells had bundled fibers of varying sizes up to 100 nm in diameter, which we will refer to as *macrofibrils* (Figure 1e,f,j). The macrofibrils reveal the three-dimensional shape of the wall, displaying wavy configurations that generally followed the indentations underlying the cuticular ridges (Figure 1e). Some *rhm1-3* cells had a moderately bundled phenotype with mostly normal-sized microfibrils and a small number of macrofibrils (Figure 1e,j), whereas others had a severely bundled phenotype with most of the cellulose present in macrofibrils (Figure 1f,j). In a few cases, macrofibrils appeared to merge (Figure 1g). Macrofibrils were present in most *rhm1-3* cells and were observed infrequently in *rhm1-1* (Figure 1k). By number, most fibers observed by FESEM in *rhm1-3* were microfibrils (Figure 1j), but based on apparent volume, the majority of cellulose in the innermost layer of the cell wall in *rhm1-3* was contained in macrofibrils (Figure 1l).

Both microfibrils and macrofibrils in *rhm1* mutants were oriented roughly transversely, like the microfibrils of wild-type cells; however, we were unable to quantify orientation because the tissue geometry was usually ambiguous from distortions during sample preparation. In *rhm1-1* and *rhm1-3* plants expressing *RHM1* from a transgene, cellulose organization was visually indistinguishable from that of the wild type (Figure 1j,k and Figure 1h,i) indicating that the cellulose organization defects were caused by mutations in *RHM1*, although statistical analysis revealed different distributions of fiber widths in the rescued *rhm1-3* plants suggesting that the rescue was not complete.

Cellulose aggregates during development in *rhm1*

FESEM requires dehydrated samples, which do not alter wall architecture in most cases (Marga et al., 2005) but can potentially cause artifacts such as kinking of cellulose microfibrils (Zhang et al., 2016). As a distinct method of analyzing cellulose organization, we stained live hydrated petals with Pontamine fast scarlet 4B, a dye that preferentially binds to cellulose (Anderson et al., 2010), and observed the petals by Airyscan super-resolution confocal microscopy (Wu & Hammer, 2021). Wild-type adaxial petal cells had mostly uniform staining (Figure 2a). The wall directly underneath the cuticular ridges stained more brightly than the intervening regions (Figure 2a), likely because the wall is indented (Figure 1b), and therefore, a greater amount of wall material is being observed when imaging perpendicularly to the cell face. Within the limit of resolution, we did not observe any aggregation of cellulose microfibrils in the wild type. By contrast, *rhm1-1* conical petal epidermal cells had obvious cellulose aggregation, with bright striations running roughly perpendicular to the cuticular ridges in most cells (Figure 2b). In plants homozygous for the phenotypically stronger alleles *rhm1-2* and *rhm1-3*, cells had substantial aggregation of cellulose, with staining in nearly all cells consisting primarily of bright striations running roughly perpendicular to the cuticular ridges (Figure 2c,d). The bright striations seen by fast scarlet staining were unaffected by pectolyase digestion, consistent with them being primarily aggregated cellulose and not pectins (Figure S1).

Petals cease cell division and enter a period of rapid expansion at the beginning of stage 12 (Huang & Irish, 2015; Irish, 2008), with the epidermal cells having formed their distinctive conical shape by stage 14 when the mature flowers are fully open (Smyth et al., 1990). In *rhm1-3* plants, petal conical epidermal cells are radially symmetric at the onset of expansion but become helically twisted by the time expansion is complete (Saffer et al., 2017). To investigate how cellulose organization changes during this period, we stained *rhm1-3* petals at different

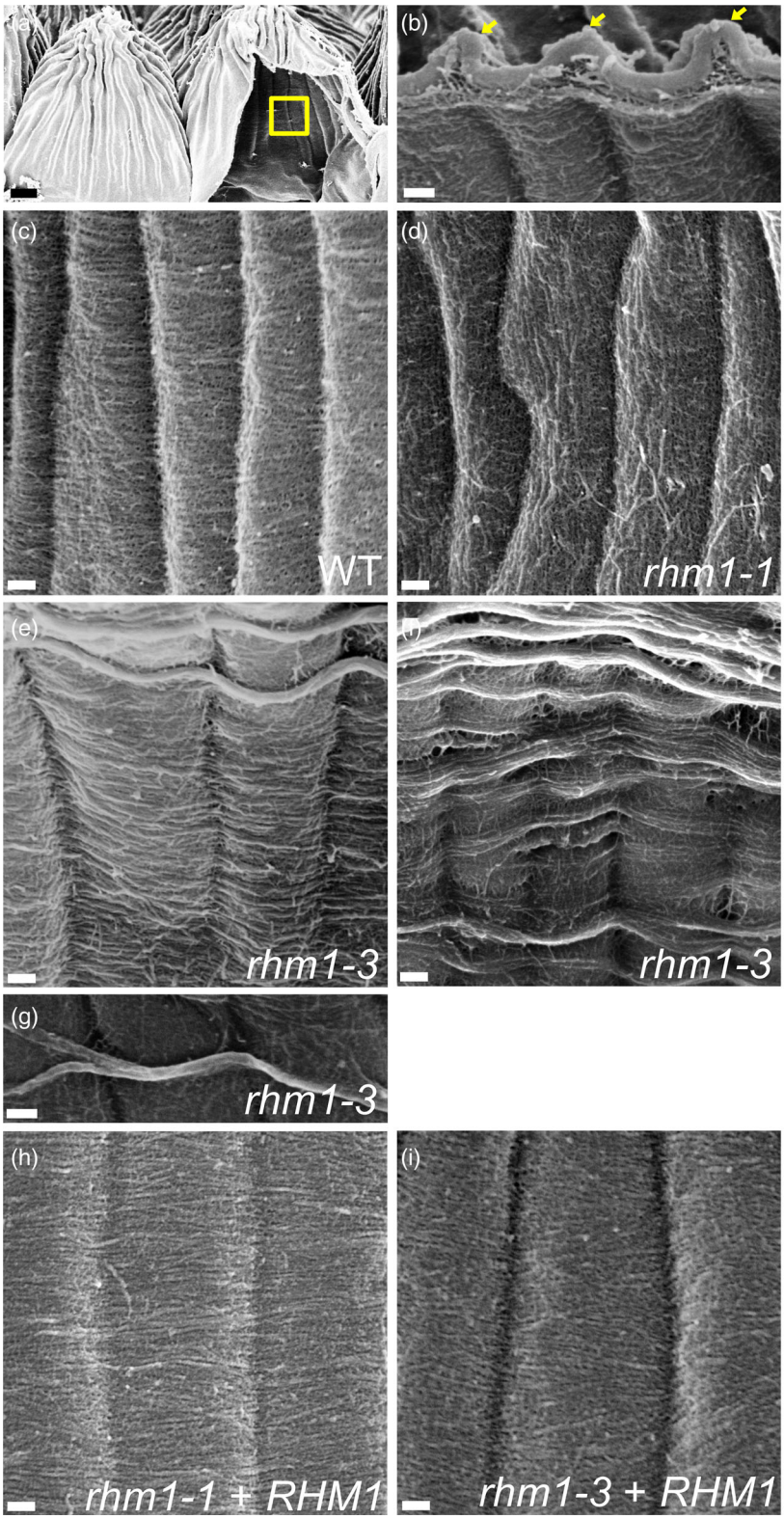

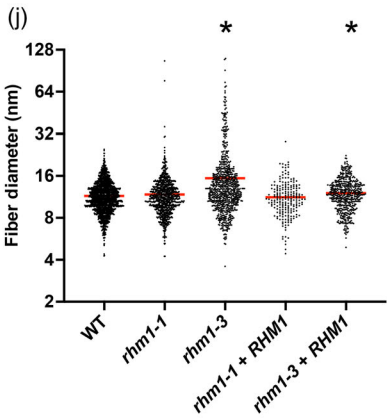

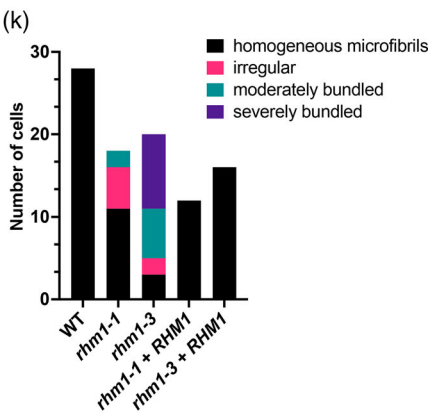

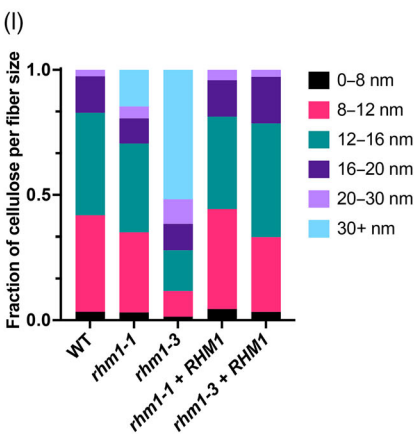

Figure 1. Mutations in *RHM1* cause cellulose bundling.
(a–i) FESEM images. (a) Petal cells were cut open and the interior surface of the cell wall (as indicated by the yellow box) of adaxial petal cells was exposed for imaging. (b) Magnified view of a cut edge of a wild-type petal cell. Cuticular ridges are marked by yellow arrows and form folds in the cuticle with the underlying cell wall indented. (c) Wild-type cells with approximately transversely oriented microfibrils and relatively homogenous fiber sizes. (d) An *rhm1-1* cell with irregularly oriented microfibrils. (e) Moderately bundled *rhm1-3* cell with two macrofibrils. (f) Severely bundled *rhm1-3* cell with many macrofibrils. (g) Higher magnification view of an *rhm1-3* cell showing two macrofibrils merging. (h) An *rhm1-1* mutant plant carrying an *RHM1* genomic transgene. (i) An *rhm1-3* mutant plant carrying an *RHM1* genomic transgene. Bars = 1 μm in (a) and 100 nm in (b–i). (j) Fiber diameters for the indicated genotypes. Each dot represents the diameter of a single fiber. The horizontal red line indicates the mean fiber diameter. The number of fibers measured was 1724 for WT, 842 for *rhm1-1*, 749 for *rhm1-3*, 212 for *rhm1-1* + *RHM1*, and 516 for *rhm1-3* + *RHM1*, from the total number of cells indicated in panel K. *Indicates equal distribution of fiber widths with the wild type is rejected at $P < 0.0001$ (Kolmogorov–Smirnov test). (k) Distribution of cells shows a wild-type phenotype with transverse microfibrils, weak mutant phenotypes with irregular arrangements of microfibrils, moderate mutant phenotypes with a few bundled macrofibrils, or severe mutant phenotypes with many large macrofibrils. (l) The fraction of cellulose in fibers of each size range was calculated assuming that the amount of cellulose was proportional to the square of fiber width.

developmental stages with fast scarlet. In early stage 12 petals, the staining was mostly uniform, and only occasional distinct striations were observed (Figure 2e). Thin and narrowly spaced striations were consistently distinguishable by the middle of stage 12 (Figure 2f) and became brighter and more separated in late stage 12 and stage 13 (Figure 2g,h). By stage 14, the mature petals had very bright striations with low signal in between (Figure 2i). Overall, the distribution of staining became less uniform throughout petal development (Figure 2j; Figure S2), indicating that cellulose increasingly aggregated during cell expansion. Compared with stage 14 petals, the striations in younger petals were more closely spaced and appeared to be more numerous. We quantified the number of distinguishable striations in the oldest stage 14 flower examined from each inflorescence and also the second-oldest flowers which were either stage 13 or late stage 12 (striations in petals younger than that were too closely packed to accurately quantify). There were more striations in the younger petals, consistent with cellulose forming fewer but larger macrofibrils as the petal developed (Figure 2k).

Cellulose aggregation is only seen in *rhm1* mutant cells with morphological defects

In *rhm1* mutant petals, epidermal cells of the abaxial blade (i.e., on the opposite side as studied above) are not twisted but do have aberrant morphology, while the longitudinally elongated claw cells at the base of the petal appear phenotypically normal (Figure S3a,b; Saffer et al., 2017). Confocal microscopy of fast scarlet-stained petals revealed no apparent cellulose aggregation in wild-type abaxial blade cells (Figure S3a). Conversely, *rhm1-3* abaxial blade cells had obvious cellulose aggregation, with bright striations running roughly perpendicular to the cuticular ridges (Figure S3b). In the petal claw, both wild-type and *rhm1-3* cells were similar, with mostly uniform staining except for increased intensity corresponding to the cuticular ridges and slight striations perpendicular to the cuticular ridges (Figure S3c,d). Two other mutants affecting pectic polysaccharides, namely *mur1* with abnormal RG-II structure (O'Neill et al., 2001) and *quasimodo2 (qua2)* (Mouille et al., 2007) with decreased levels of homogalacturonan, do not cause helical twisting of petals (Saffer et al., 2017); neither mutant displayed any evident cellulose aggregation in the adaxial petal blade cells (Figure S3e–g). Plants with mutations in *spiral2 (spr2)*, which encodes a microtubule-associated protein (Fan et al., 2018), have right-handed twisting of multiple organs including petal claws (Figure S3h,i) as a consequence of altered microtubule orientation (Furutani et al., 2000) but did not show increased cellulose aggregation as compared with the wild type (Figure S3j,k).

Crystalline cellulose in petals is decreased in *rhm1* mutants

To determine whether *rhm1* mutants have defects in overall cellulose levels, we measured crystalline cellulose in petals as the amount of carbohydrate resistant to acetic and nitric acid (Updegraff, 1969). All alleles of *rhm1* had less crystalline cellulose than the wild type, with both of the stronger alleles *rhm1-2* and *rhm1-3* having significant decreases (Figure 3). Therefore, *rhm1* mutants affect crystalline cellulose levels, either by altering the fraction of amorphous cellulose that is sensitive to acid digestion or by impairing cellulose synthesis.

Microtubules are unlikely to initiate helical twisting of *rhm1* petals

To test if altered microtubule orientation could cause the helical twisting of *rhm1* petals, we observed microtubule organization in developing conical petal epidermal cells. At the beginning of stage 12 in the wild type, microtubules were either oriented transversely or were seemingly disorganized (Figure 4). As the cells expanded, the microtubules became oriented circularly in concentric hoops around the cone, consistent with how microtubules would be expected to orient in response to the stress from conical expansion (Hamant et al., 2008) and consistent with the transverse orientation of cellulose (Figure 1c). Initially, *rhm1-3* cells had a similar microtubule arrangement as the wild type with a mix of transverse and relatively disorganized microtubules (Figure 4). Unlike in the cells of helically twisted microtubule mutants, *rhm1-3* petal microtubules did not become arranged in well-ordered

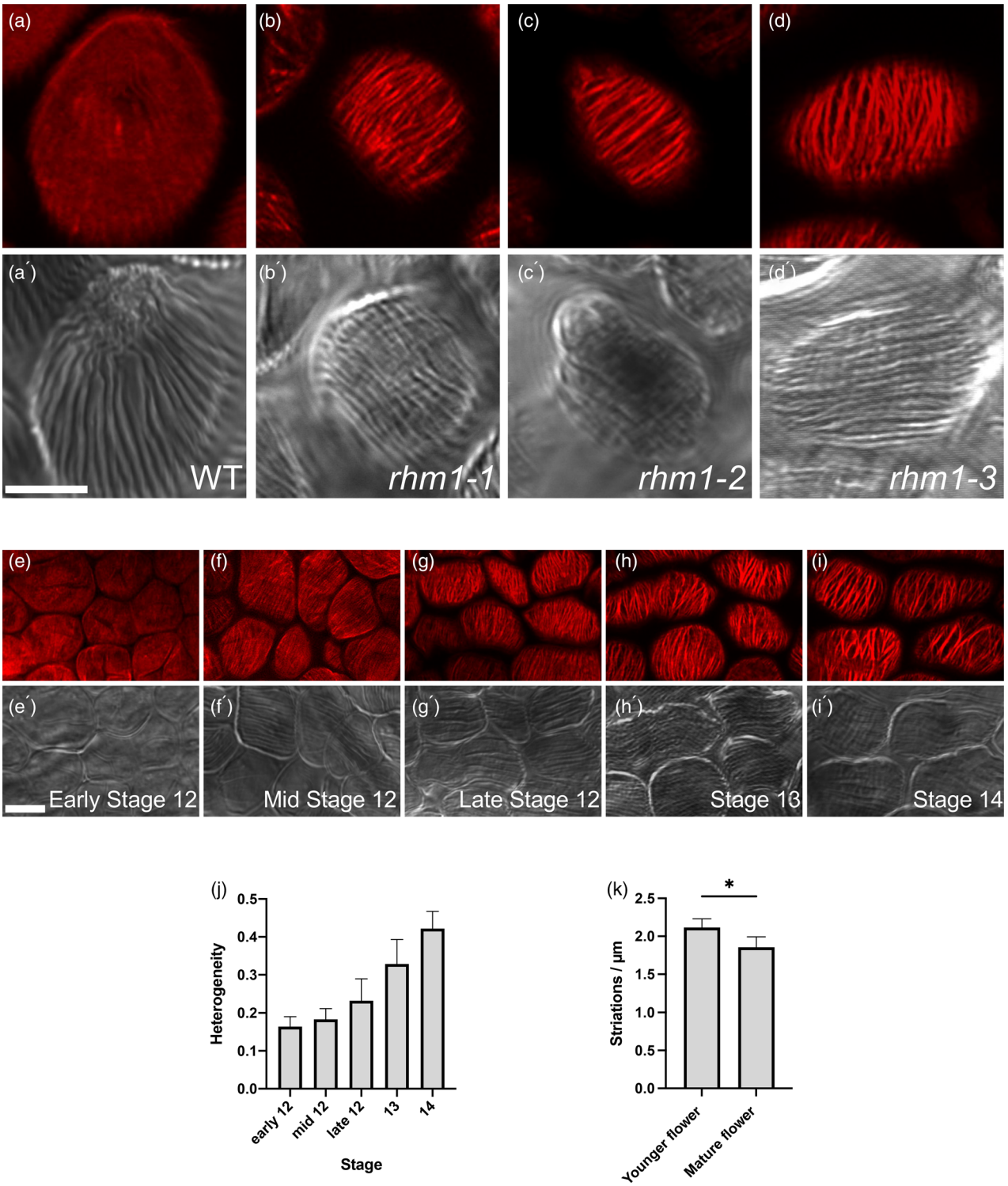

Figure 2. Cellulose aggregates during cell expansion in *rhm1* mutant petals.
Petals were stained with fast scarlet and imaged by Airyscan confocal microscopy. (a–d) Representative images of fast scarlet staining in stage 14 conical petal epidermal cells of the indicated genotypes. (a′–d′) Differential interference contrast (DIC) images corresponding to (a–d). (e–i) Time course of conical petal cell development in *rhm1-3* from the beginning of stage 12 at the onset of rapid cell expansion to a mature stage 14 petal. (e′–i′) DIC images corresponding to (e–i). Bars = 5 μm. (j) Heterogeneity of cellulose staining (see Figure S2) in *rhm1-3* during petal development (n = 4 inflorescences). Heterogeneity was correlated with the stage ($P < 0.05$ by Spearman's rank correlation). (k) Striation density in *rhm1-3* petal cells over time. For each inflorescence (n = 4), the number of distinct striations was quantified for petal cells from both a mature stage 14 flower and the next younger flower. * Indicates equal density of striations for the two flower types is rejected with $P < 0.05$ (by t-test). In (j) and (k), bars plot mean ± standard deviation.

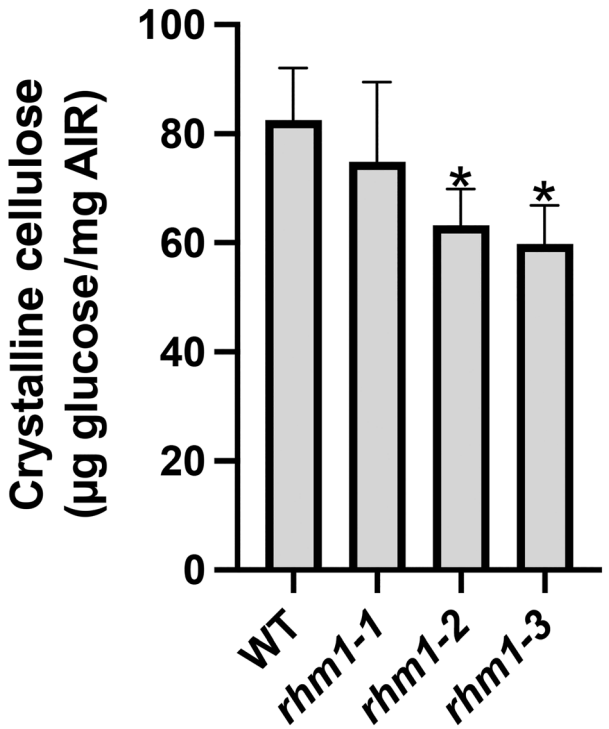

Figure 3. Decreased levels of crystalline cellulose in *rhm1* mutants.
Crystalline cellulose levels in petals measured by Updegraff assay. Bars plot mean ± standard deviation. Four biological replicates were assayed for each genotype. * Indicates equality with the wild type is rejected at $P < 0.05$ (*t*-test).

helical arrays. In older *rhm1-3* petals, some cells adopted a hoop-like microtubule arrangement, whereas others did not, likely because most *rhm1-3* cells fail to undergo substantial conical cell expansion.

Cellulose adopts a right-handed helical organization in *rhm1* mutants

The cellulose bundling of *rhm1* mutants raises the possibility that their helical growth might result from chiral cellulose organization on a cellular scale. We imaged sections of petals by polarized-light microscopy, taking advantage of the intrinsic birefringence of cellulose. Orientation could be assayed where the section plane passed through the side wall of a cone, preserving tissue geometry. In wild-type petals, cell walls had largely uniform birefringence retardation (also called retardance) consistent with nonaggregated microfibrils, whereas in *rhm1-3* petal cell walls, the pattern of retardance was striated, similar in appearance to fast scarlet staining (Figure 5b). We quantified the orientation of the optic axis of the birefringent elements, which corresponds to the net orientation of cellulose, projected into the object/image plane, with the long axis of the cone defined as ±90° (Figure 5a). Cellulose organized helically around a cell will form an oblique angle when one side of a cell is observed (Figure 5a). The net orientation of cellulose was on average closer to the transverse in the wild type and more evidently helical in *rhm1-3* (Figure 5d). A limitation of our preparation is that it was unclear whether the imaged cell wall was being observed from the inside or outside of the cell and so we could not tell whether a nontransverse alignment represented a left- or right-handed helical structure. This inability to determine the geometry of the cell means that measured orientations were the absolute value of the real orientations.

To assess cellulose orientation in a manner that preserves cell geometry and handedness, we made use of the fact that upon binding to cellulose, fast scarlet becomes co-aligned with the cellulose; therefore, fluorescence intensity varies as a function of the polarization of the exciting light (Thomas et al., 2017). We quantified the orientation of fast scarlet, and hence cellulose, by evaluating fluorescence in response to excitation at four defined angles of linear polarization (Spira et al., 2017). The fluorescence signals from wild-type and *rhm1* mutant conical petal epidermal cells were anisotropic, consistent with well-ordered cellulose (Figure 5c). Cellulose orientation was calculated for a single face of the cell wall as viewed from the outside of the cell, thereby distinguishing between left- and right-handed helical orientations (Figure 5a). Cellulose in wild-type conical petal cells was on average transverse, with no bias toward left- or right-handed orientations (Figure 5e; Figure S4). By contrast, in *rhm1-1*, cellulose orientation shifted toward right-handed alignment, with the average cell having cellulose oriented 5° from transverse (Figure 5e). In *rhm1-3*, the shift was larger (on average 11°), and nearly every cell had a right-handed cellulose orientation (Figure 5e). In Figure 5e, the measured angles for *rhm1-3* were on average smaller than in panel Figure 5c, likely because the intact preparation allowed the petal cone axis to be determined more reliably. Thus, in *rhm1* mutant cells, cellulose was oriented into right-handed helices around the cell, with the cells of the more severe mutant having a steeper helicity.

Helical twisting of *rhm1* petal cells is enhanced by increased cell size

To test whether altered cell expansion influences the degree of cell twisting, we generated tetraploid wild-type, *rhm1-1*, and *rhm1-3* plants and octoploid *rhm1-1* plants. Polyploid plants had substantially larger petals than diploid plants (Figure S5a), and polyploidization increased the height of conical petal epidermal cells, although the magnitude of the effect differed between genotypes (Figure 6b; Figure S5b). Tetraploid *rhm1-1* petal cells were substantially taller than in the corresponding diploid, and in the octoploid *rhm1-1* these cells were even larger. Conversely, tetraploid *rhm1-3* petal cells were only slightly taller than in the *rhm1-3* diploid, and both were shorter than in the

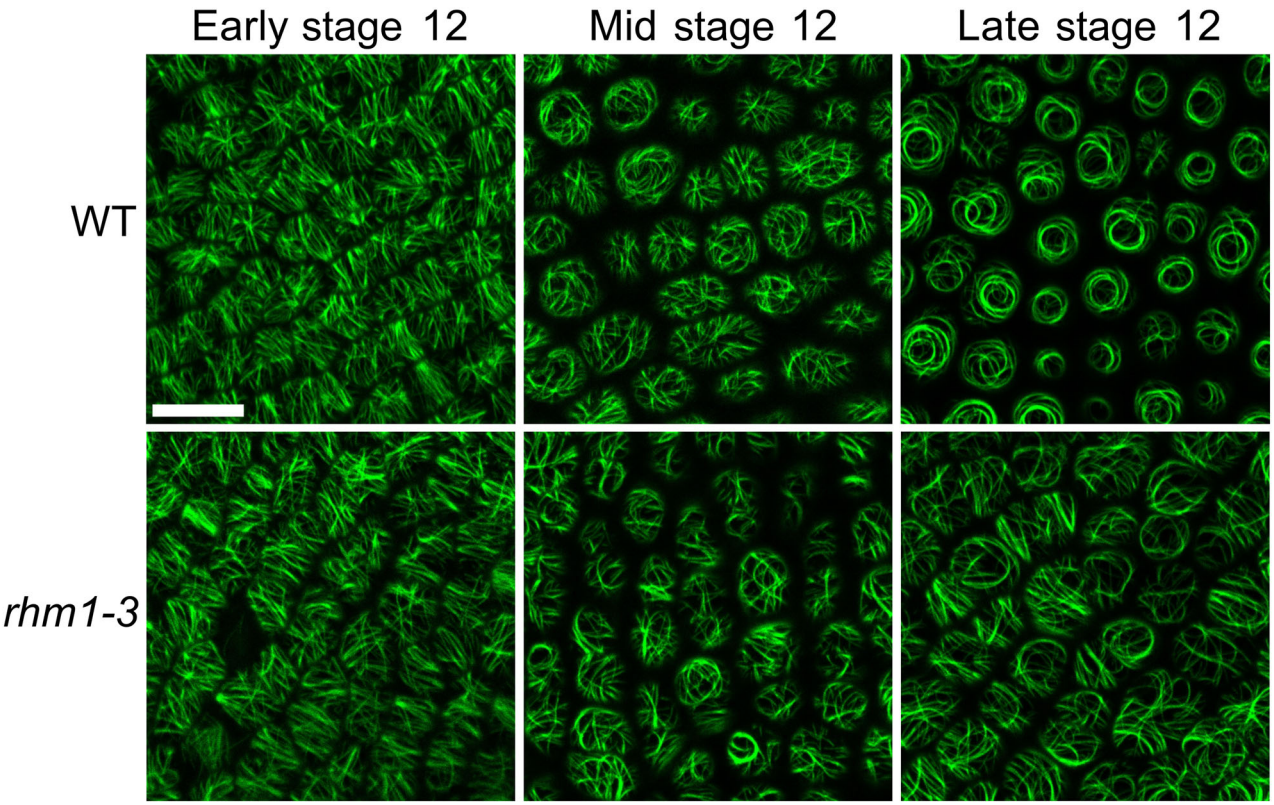

Figure 4. Microtubule organization in conical petal cells.
Microtubules were imaged in expanding stage 12 adaxial conical petal epidermal cells using a reporter line with fluorescently tagged alpha-tubulin. Representative images are shown for each genotype and stage. Bar = 10 μm.

wild type (Figure 6b). The conical petal epidermal cells of both diploid and tetraploid *rhm1-3* twisted to a negligible extent; however, in *rhm1-1*, increasing ploidy was accompanied by a greater proportion and severity of cell twisting (Figure 6a,c). Cell walls from diploid *rhm1-1* and *rhm1-3* flowers contained 20 and 30%, respectively, less rhamnose than diploid wild-type cell walls, and the tetraploid *rhm1* mutants had similar cell wall monosaccharide composition as the corresponding diploids (Figure S5c), indicating that tetraploidization did not substantially modify the effects of *rhm1* mutations on cell wall composition. Together these results indicate that the degree of helical twisting increased with increasing cell height.

DISCUSSION

Using several experimental approaches, we have shown that cellulose assembles into macrofibrils in *rhm1* mutant petals (Figures 1 and 2; Figure S3). In these cells, macrofibrils were revealed by FESEM imaging of the most recently deposited cellulose on the innermost cell wall (Figure 1). However, there were also many normal-size microfibrils, indicating that *rhm1* mutants can still synthesize normal microfibrils and that the altered pectin composition does not substantially change the thickness of the matrix polysaccharide coating around the microfibrils (Figure 1j). Compared to FESEM, imaging cellulose through the entire cell wall thickness by birefringence or fast scarlet staining showed a higher prevalence of cellulose aggregation, with nearly all *rhm1* conical petal cells having striations, indicating that older cellulose molecules are bundled to a greater degree than freshly deposited ones. Although the optical approaches could show more cellulose aggregations relative to FESEM because they integrate multiple cell wall layers, the high frequency of aggregated cellulose observed by optical approaches, especially in the *rhm1-1* mutant, combined with the thinness of the petal walls, suggests that cellulose aggregation is greater in deeper cell wall layers compared with the surface. Consistent with cellulose aggregating postsynthetically, cellulose was organized in fewer but brighter striations as petals matured (Figure 2). Overall, our data indicate that cellulose microfibrils are synthesized normally in *rhm1* mutants and then progressively bundle into macrofibrils.

Cellulose bundling suggests *rhm1* cell walls lack a component that prevents cellulose self-association. *RHM1* encodes a UDP-L-rhamnose synthase, which supplies rhamnose for various macromolecules (Diet et al., 2006; Oka et al., 2007). In *Arabidopsis thaliana*, the macromolecules

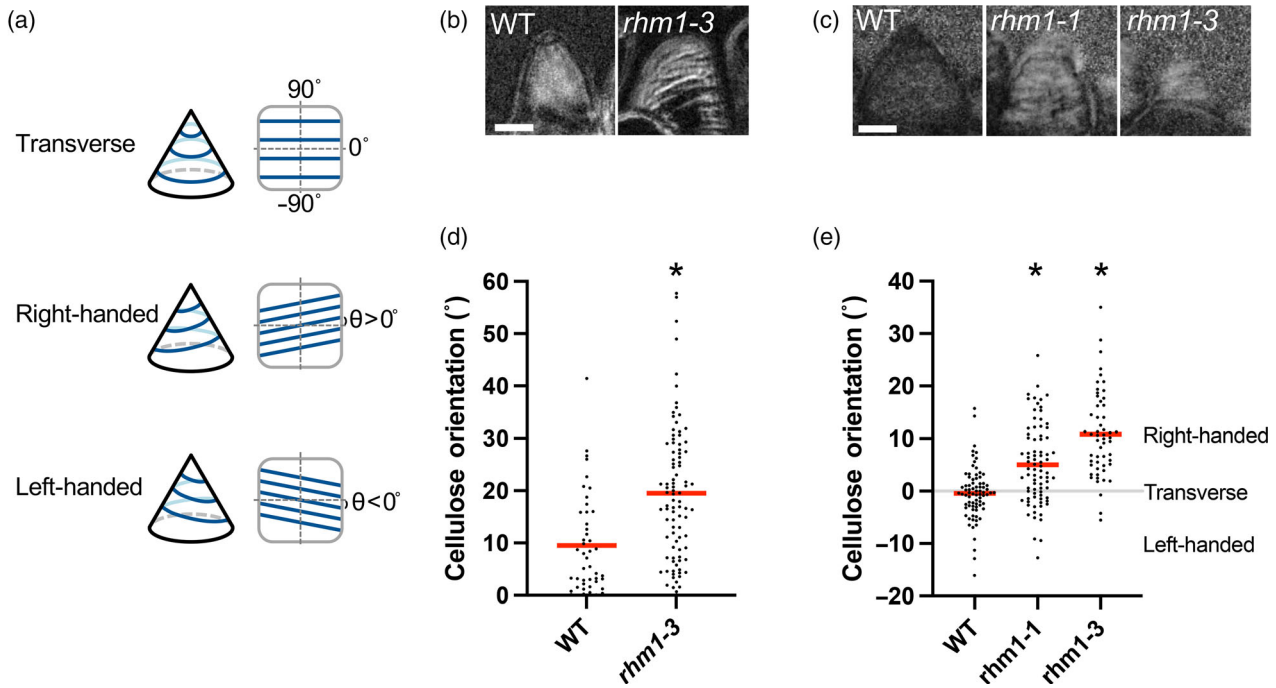

Figure 5. Conical petal epidermal cells in *rhm1* have right-handed helical cellulose.
(a) Diagrams on the left show cones with transverse or helically oriented cellulose, with darker blue representing cellulose on the near side of the cone and lighter blue representing cellulose on the far side of the cone. Diagrams on the right show how the cellulose would appear when a region of the near wall is viewed from outside the cell, with 0° representing a transverse orientation, values less than 0° representing left-handed helices, and values greater than 0° represent right-handed helices. (b) Birefringence retardation in conical petal epidermal cells. (c) Fluorescence anisotropy of fast scarlet-stained conical petal epidermal cells, with brighter pixels indicating higher anisotropy. In b and c, intensity is proportional to retardance (b), or fluorescence anisotropy (c), regardless of the orientation of the anisotropic elements. Bars = 5 μm. (d) Average of the absolute values of the optical axis of birefringent elements relative to the axis of the conical cells. Cellulose is positively birefringent so the optical axis corresponds to the long axis of the microfibril. Each dot represents a measurement from one cell, and the horizontal red line indicates the mean, with $n = 45$ cells from two flowers for wild type and 92 cells from two flowers for *rhm1-3*. (e) Orientation of cellulose measured by polarized confocal microscopy of fast scarlet-stained conical petal epidermal cells with $n = 78$ cells from five flowers for wild type, 81 cells from eight flowers for *rhm1-1*, and 55 cells from seven flowers for *rhm1-3* (see also Figure S4). Each dot represents a single cell, with the horizontal red line indicating the mean. * Indicates equality with the wild type is rejected at $P < 0.0001$ (*t*-test).

that contain rhamnose are primarily the pectins RG-I and RG-II, and rhamnosylated flavonols (Atmodjo et al., 2013; Jones et al., 2003; Yonekura-Sakakibara et al., 2007, 2008). RG-I levels are decreased in *rhm1*, while a mutant impairing RG-II function does not cause helical growth, and rhamnosylated flavonols are not required to prevent helical growth (Saffer et al., 2017; Saffer & Irish, 2018). Therefore, RG-I itself is likely responsible for maintaining dispersed microfibrils, although we cannot rule out the possibility that an unknown rhamnose-containing matrix polysaccharide is responsible or that diminished RG-I induces novel compensatory reactions.

Pectins are known to closely associate with cellulose, possibly through RG-I, based on NMR spectroscopy (Dick-Perez et al., 2011; Wang et al., 2012, 2015) and binding experiments with purified components (Lin et al., 2016; Zykwinska et al., 2005, 2007). Also, cellulose macrofibrils are abundant in secondary cell walls, which have little or no pectin (Donaldson, 2007; Lyczakowski et al., 2019), consistent with a role for RG-I in preventing cellulose bundling. Previous work implicated pectins, and particularly homogalacturonan, in influencing cellulose architecture, but none of those examples reported helical cellulose arrangement, suggesting that, among pectins, RG-I has a specific role in blocking chiral assembly of cellulose (Du et al., 2020; Thimm et al., 2009; Yoneda et al., 2010). Most mutants known to cause helical growth do so by altering microtubule orientation (Smyth, 2016), but it would be interesting to investigate if the few helical growth mutants that do not appear to act through microtubules (Sedbrook, 2002) affect cellulose architecture or bundling.

Macrofibrils sometimes occur in wild-type primary cell walls (Anderson et al., 2010; Ding & Himmel, 2006; Sugimoto et al., 2000; Zhang et al., 2016), but in these cases, the magnitude and prevalence of bundling is much less than in *rhm1* petals. These examples of occasional macrofibrils are not associated with inhibited growth, while *rhm1* mutant petal conical cells are smaller than wild-type cells (Figure 6b; Figure S5b), suggesting that excessive cellulose bundling impairs cell expansion.

Cellulose becoming both bundled and organized into helical arrays raises the possibility that the bundling of cellulose itself creates the cellular scale chirality. Elementary cellulose microfibrils have an intrinsic right-handed twist

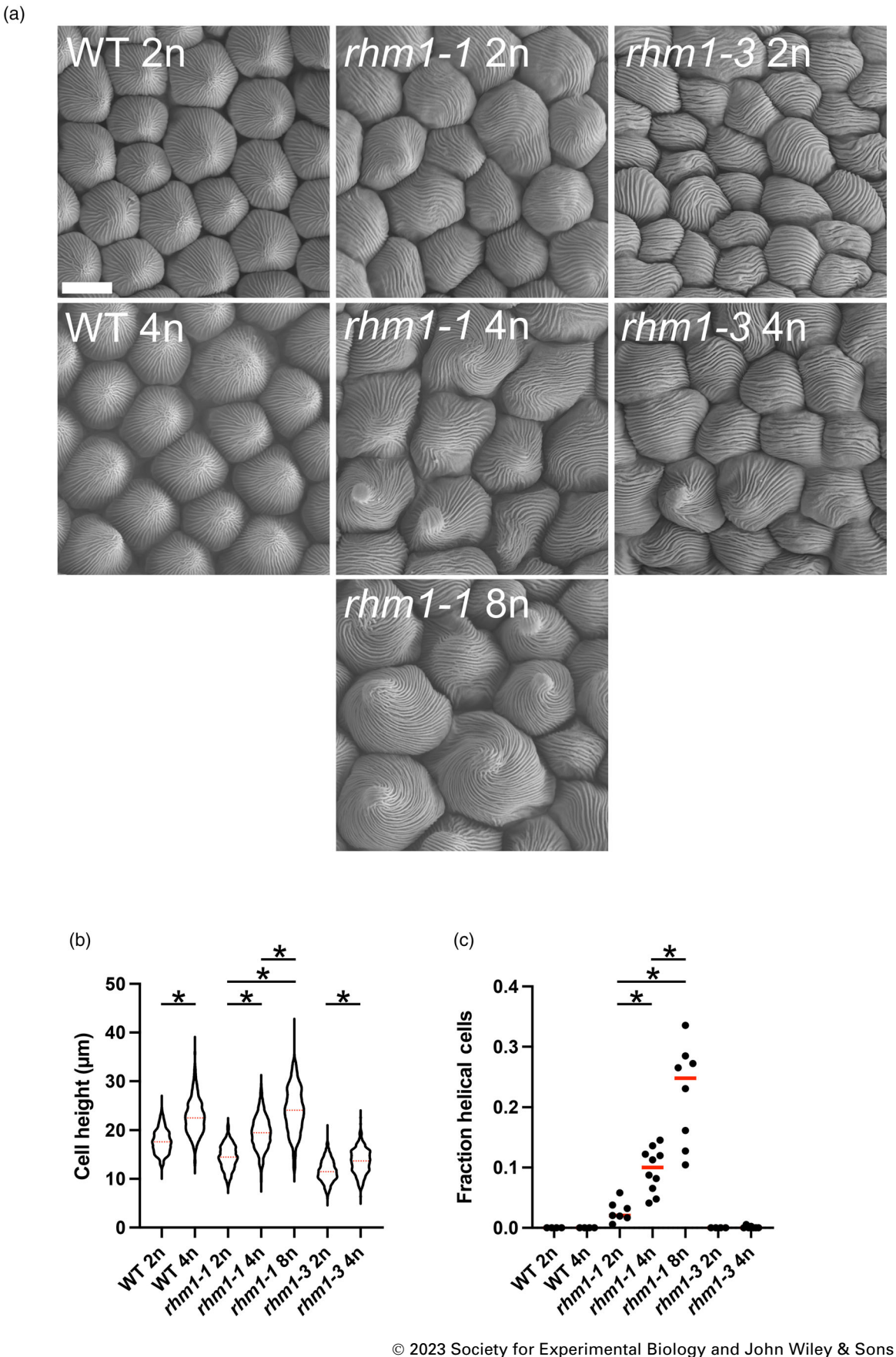

Figure 6. Polyploid *rhm1* petals cells are larger and more twisted than in the corresponding diploid mutants.
(a) Scanning electron microscope images of conical petal epidermal cells from diploid (2*n*), tetraploid (4*n*), or octoploid (8*n*) plants. Bar = 10 μm. (b) Violin plots of petal epidermal cell heights measured from sectioned petals. At least 340 cells from a minimum of 8 flowers were assayed for each genotype. The dotted red line represents the median height. (c) The fraction of cells with obvious helical twisting in scanning electron microscope images. At least 60 cells from a minimum of four flowers were assayed for each genotype. Each dot is the fraction of twisted cells in one flower, and the horizontal red line indicates the median. * Indicates equality between plants of different ploidy with the same genotype is rejected at $P < 0.0005$ (*t*-test).

along their axis, as demonstrated by ultrastructural observation (Hanley et al., 1997, p. 199; Usov et al., 2015) and molecular modeling (Matthews et al., 2006; Paavilainen et al., 2011). Interactions between chiral molecules can create larger-scale chiral structures, although the exact relationship between molecular and mesoscale chirality is complicated and depends on the density and the precise nature of the chiral molecules (Belli et al., 2014; Morrow et al., 2017). Empirically, it is known that cellulose is intrinsically capable of assembling into structures of consistent chirality. Cellulose nanocrystals formed by weak acid-hydrolysis of cellulose self-assemble into a chiral nematic phase *in vitro* in which the cellulose forms well-aligned layers, with each layer rotated slightly to form a left-handed helicoidal structure (Majoinen et al., 2012; Revol et al., 1992). Although helicoids formed *in vitro* by cellulose nanocrystals differ structurally from the helical cellulose macrofibrils formed in *rhm1*, we argue that these structures similarly emerge from the intrinsic chirality of cellulose and the consequent tendency for such molecules to interact in a chiral manner; the manifestation of that chiral interaction will depend on both the length of the cellulose molecules and their environment.

Helically oriented cellulose is necessary to drive helical cell expansion but a twisted morphology arises only when a cell expands sufficiently, as seen with the stunted *rhm1-3* conical petal epidermal cells that rarely twist despite having helical cellulose. This growth requirement is likely because of the mechanism by which helically oriented cellulose causes helical cell expansion of the opposite handedness: the mechanically chiral wall twists as it expands (Chakraborty et al., 2021; Probine, 1963; Smyth, 2016; Wada & Matsumoto, 2018). The decreased petal cell expansion in severe *rhm1* alleles might be insufficient for such twisting to occur; in fact, bundled macrofibrils might generally limit cell wall deformation. We hypothesize that cell twisting in conical petal epidermal cells reflects a narrow optimum in which cellulose has become sufficiently helical to alter cell expansion but before expansion and twisting becomes blocked by excessive cellulose bundling.

Beyond the minimal level of growth required for cellular twisting, cell expansion might amplify the extent of helical twisting arising from chiral cellulose interactions for two reasons. First, by analogy to the chiral nematic phase of cellulose nanocrystals where each layer is only rotated by a very small amount (Schütz et al., 2015), any individual interaction between two cellulose fibrils in the cell wall is expected to impart only a small amount of helicity to the cellulose organization, and therefore pronounced helicity would require the accumulation of many such slightly twisted interactions. Assuming a constant wall thickness, increased cell expansion would require more cellulose synthesis and thereby increase the number of these interactions, resulting in more strongly helical cellulose. Second, if newly synthesized microfibrils adhere to preexisting cellulose, then passive reorientation caused by cell expansion would progressively steepen the pitch of the cellulose helix (Chakraborty et al., 2021). The enlarged conical petal epidermal cells of polyploid *rhm1-1* mutants had substantially more helical twisting than the corresponding diploid (Figure 6), consistent with a model in which many slightly chiral interactions between cellulose molecules eventually lead to a mesoscale helical cellulose architecture and hence helical growth.

Left-handed helical twisting of cells and organs arises from decreased levels of the pectin, RG-I (Saffer et al., 2017). On a much smaller scale, D-glucose is a chiral monosaccharide, and cellulose has uniform chirality in molecular structure, macromolecular shapes, and in higher-order structures formed by interacting cellulose molecules (Hanley et al., 1997; Revol et al., 1992; Usov et al., 2015). Here, we connect these length scales by demonstrating that when RG-I levels are decreased, cellulose bundles into chiral mesoscale structures that lead to cellular chirality, showing how chirality can be transferred across widely different length scales in a biological system and demonstrating that the interplay between distinct cell wall components is required to mask that chirality.

EXPERIMENTAL PROCEDURES

Growth conditions

Plants were grown in a mix of two parts vermiculite to one part either Fafard Superfine Germinating Mix or PRO-MIX BX soil at 22°C with 16 h of 150 μmol m^{-2} sec^{-1} light per day. All staging of flowers was done as described (Smyth et al., 1990). Unless otherwise noted all experiments were performed on adaxial conical epidermal cells from the distal blade region of the petal from mature stage 14 flowers.

Genetic material

All experiments were performed in the *Arabidopsis thaliana* Columbia (Col-0) background unless stated otherwise. Three

alleles of *RHM1* were used; for clarity, we refer to them as *rhm1-1*, *rhm1-2*, and *rhm1-3*. Originally, *rhm1-1* and *rhm1-2* were named *rol1-1* and *rol1-2*, respectively (Diet et al., 2006). The *rhm1-3* mutant, which was originally isolated in a L*er* background (Saffer et al., 2017), was backcrossed six times to Col-0 before being used for these experiments. The *mur1-1* (Reiter et al., 1993) and *qua2-1* (Mouille et al., 2007) alleles were used. The *spr2-1* mutant (Furutani et al., 2000) is in a Landsberg *erecta* (L*er*) background. For transgene rescue experiments, *rhm1-1* and *rhm1-3* plants were transformed with a genomic *RHM1* construct (Saffer et al., 2017) using the floral dip method, and then flowers were processed from T_1 transgenic plants that displayed nonhelical wild-type petal morphology.

Field-emission scanning electron microscopy

Freshly removed mature stage 14 flowers were embedded in 5% low melting point agarose dissolved in water. The agarose was affixed to a metal block using superglue with the flowers pointed vertically and then mounted into a Vibratome 1000 Plus. Approximately 200–400 μm was cut off of the distal tip of each petal using a double-edged razor blade at speed 3 and amplitude 8. The flowers were then manually dissected away from the agarose. Cut flowers were placed in PBS plus 0.1% Triton X-100 with gentle agitation for 1 h to remove cytoplasm. Samples were dehydrated in an ethanol series from 10% to 100% ethanol with several changes of 100% ethanol with each dehydration step lasting a minimum of 2 h, and were then critical point dried with CO_2 in a Polaron E3000 unit. Petals were dissected from dehydrated samples and mounted on the vertical side of aluminum pin stubs with 45° and 90° angled surfaces (Electron Microscopy Sciences #75353) with the cut end of the petal pointing upwards by using NEM double-sided adhesive carbon tape (Electron Microscopy Sciences #77816). Samples were sputter coated with a thin layer of platinum using an Edwards sputter coater. Samples were imaged on an FEI Magellan 400 field emission scanning electron microscope at 2 kV accelerating voltage and 50 pA beam current at a 4 mm working distance with a through-lens detector. To measure fiber widths, for each cell the diameter of all visually distinguishable fibers intersecting a line along the vertical axis of the cone was manually measured using FIJI (Schindelin et al., 2012). To determine the distribution of cellulose by fiber size, the relative amount of cellulose in each fiber was calculated as the square of the diameter, and the relative amounts of cellulose from fibers of each indicated size range were summed.

Pontamine fast scarlet 4B staining

To render petals permeable to dye and allow the adaxial and abaxial sides to be distinguished, a corner of the distal tip of each petal was cut at an angle using a razor blade or hypodermic needle. Petals were stained with 0.1% (w/v) Pontamine fast scarlet 4B (also known as direct red 23; Sigma-Aldrich #212490) and 0.015% Silwet L-77 in water and incubated for 1 h at room temperature with gentle agitation. After staining, petals were washed several times with 0.1% Triton X-100 in water and then mounted on glass slides in the same solution, with the adaxial side facing the coverslip.

Microtubule imaging

A *pdf1*::mCitrine:*TUA6* construct expressing an mCitrine-tagged *alpha tubulin 6* gene under the control of the epidermal-specific *pdf1* promoter was constructed similarly as previously described (Armezzani et al., 2018) and transformed to Col and *rhm1-3* plants by floral dip (Clough & Bent, 1998). Two independent T_2 lines were imaged for each genotype with no qualitative differences observed between different lines in the same genotype. Petals were mounted in water with 0.1% triton and imaging was performed on a Zeiss LSM880 laser scanning confocal microscope with a 63× 1.4 NA plan apochromat oil-immersion lens at 3× optical zoom. An argon laser at 488 nm excited mCitrine and emissions were captured between 493–552 nm with a pinhole set to one Airy unit.

Pectolyase treatment

Stage 14 flowers were embedded in low melting point agarose and petals were cut transversely on a Vibratome identically to the preparation for FE-SEM. The cut flowers were placed in a microcentrifuge tube with PBS and 0.1% triton. Pectolyase Y-23 (Duchefa Biochemie) was then added to some samples at a final concentration of 1 mg/ml. Tissue with or without pectolyase was incubated at room temperature for 1 h on a rotator at approximately 40 RPM, then washed several times with PBS + 0.1% triton. Samples were then stained with Pontamine fast scarlet and prepared for microscopy as described above.

Airyscan microscopy

Petals were imaged on a Zeiss LSM880 laser scanning confocal microscope equipped with an Airyscan detector module using a 100× 1.46 NA Alpha plan apochromat oil-immersion lens. Fast scarlet was excited with an argon laser at 514 nm and detected by an Airyscan detector in super-resolution mode with BP420-480 and BP495-620 emission filters, and 1.8× optical zoom. The differential interference contrast (DIC) channel was imaged with an argon laser at 488 nm and a PMT detector. Airyscan deconvolution processing was performed with Zeiss Zen software with a filter strength of 6 in 2D mode.

For the developmental series, four *rhm1-3* inflorescences were imaged from four plants. For each inflorescence, starting from a mature stage 14 open flower, every successive younger flower was dissected in order and observed under a dissecting microscope to determine the stage of the flower, and the petals were removed and stained as described above.

To quantify the heterogeneity of cellulose distribution, we used FIJI to draw a three-pixel wide line on each cell parallel to the cuticular ridges and perpendicular to the cellulose bundles and then calculated heterogeneity of the cellulose staining as the standard deviation along that line as a fraction of the mean intensity. To quantify the frequency of distinguishable cellulose bundles, we drew a line for each cell parallel to the cuticular ridges and used the Find Peaks ImageJ plugin (Ferreira et al., 2015; http://doi.org/10.5281/zenodo.28838) to count the number of distinct peaks using a minimum peak amplitude setting of 1/20th of the mean pixel intensity along the line.

Polarized-light microscopy

Flowers were fixed in 50% ethanol, 3.7% formaldehyde, and 5% acetic acid (FAA) under vacuum infiltration for 1 h, left overnight, then dehydrated in an ethanol series. Flowers were then embedded in methacrylate essentially as previously described (Baskin et al., 1992). Briefly, fixed tissue was infiltrated with increasing concentrations of a methacrylate solution consisting of 80% butyl methacrylate and 20% methyl methacrylate and then placed into a degassed solution of 80% butyl methacrylate, 20% methyl methacrylate, 0.5% benzoin methyl ether, and 10 mM dithiothreitol (DTT) in BEEM capsules. Methacrylate was polymerized for 4 h with a UV light box. A Sorvall MT-2 ultramicrotome with a glass knife

was used to cut two μm thick transverse sections which were placed on glass slides coated with 3-aminopropyltriethoxysilane, mounted in 50% glycerol, and sealed with a coverslip and nail polish. Sections were imaged on a Nikon Microphot SA microscope stand configured as an LC-PolScope, as described (Oldenbourg & Mei, 1995). The liquid crystal universal compensator was manufactured by Cambridge Research and Instrumentation, now part of PerkinElmer, Waltham MA. Cells were viewed using a strain-free 60×, 1.4 NA oil immersion plan apo objective lens, and digital images were captured using a Q-Imaging Retiga 2000R camera and processed using a Java-based image processing system for calculating images of birefringence retardation and slow axis orientation (OpenPolScope system, https://openpolscope.org). Net cellulose orientations are reported as the absolute value of angles relative to the long axis of the conical portion of the epidermal cell.

Polarized fluorescence confocal microscopy

Petals were stained with fast scarlet as described above. Stained petals were folded in half on the microscope slide, with the fold as close as possible to the cut distal tip, such that the adaxial petals cells were protruding along the crease and allowing imaging of the conical cells in a profile view. Petals were mounted in 0.1% Triton X-100 in water. Petals were examined on a Zeiss LSM780 laser scanning confocal microscope equipped with a liquid-crystal universal compensator (Meadowlark Optics, Frederick CO) controlled by OpenPolScope software (Spira et al., 2017). Fast scarlet was excited with a 561 nm laser and observed through a 40× 1.2 NA C-apochromat water immersion lens at 2.6× zoom. Z-stacks were obtained with 1 μm spacing to span the depth of the conical cells. Each Z-position was imaged in four different polarizer orientations, and the Pol-analyzer plug-in was used to measure the apparent orientation of the chromophore dipole, as previously described (Spira et al., 2017). The orientation of the fluorescence was measured for the conical face of the petal cells and compared to the conical axis of the cell to determine the orientation of the cellulose.

Crystalline cellulose measurements

Approximately 10 mg fresh weight of petals were collected for each sample and lyophilized. Cell walls were isolated as the alcohol-insoluble residue (AIR) after extraction twice with 70% ethanol at 60°C for 1 h each with occasional vortexing, and then with 100% ethanol, 100% methanol, and 100% acetone sequentially for 30 min each at room temperature on a rotator at 40 RPM. AIR was then dried and weighed. Crystalline cellulose content was measured using the Updegraff method (Updegraff, 1969). AIR was hydrolyzed with a mix of 8 parts acetic acid:2 parts water:1 part nitric acid at 100°C for 30 min, and the pellet was washed repeatedly with water and 100% acetone and then dried. A solution of 0.7% anthrone in 70% sulfuric acid was added to each sample and placed at 100°C for 5 min. The amount of carbohydrate in each sample was determined by measuring the absorbance at 620 nm and comparing it with a standard curve of glucose concentrations.

Generation of polyploid plants

Seven-day-old seedlings grown on plates with half-strength Murashige and Skoog (MS) salts, 1% (w/v) sucrose, and 0.8% (w/v) agar were submerged in an aqueous solution of 0.005% (w/v) colchicine (Alfa Aesar) for 2 h and then washed many times with water. Seedlings were allowed to grow for six more days on plates and then transplanted to soil. Putative polyploid plants were identified in the next generation by the number of branches on trichomes, and then the ploidy of tetraploid and octoploid plants was confirmed in rosette leaves by flow cytometry as previously described (Dong et al., 2021).

Measurement of cell height

Flowers were embedded in 5% low melting point agarose dissolved in water, cut into 200 μm thick sections with a Vibratome 1000 Plus using a double-edged razor blade at speed 3 and amplitude 8, stained with toluidine blue, and then imaged at 40× magnification on a Zeiss Observer D1 microscope. Cell heights were measured using FIJI.

Scanning electron microscopy

Flowers were fixed in 50% (v/v) ethanol, 3.7% (v/v) formaldehyde, and 5% (v/v) acetic acid (FAA) overnight, dehydrated in an ethanol series, and then critical point dried with CO_2. Flowers were mounted on aluminum stubs with carbon conductive tape and sputter coated with an approximately 15 nm thick layer of either gold or platinum. Tissue was viewed with a Hitachi SU7000 scanning electron microscope at an accelerating voltage of 10 kV.

Monosaccharide composition analysis

Mixed-stage whole flowers were lyophilized and then homogenized for 2 min at 25 Hz in a QIAGEN TissueLyser with a 5 mm steel ball, producing approximately 20 mg tissue per sample by dry weight. To prepare alcohol insoluble residue (AIR), samples were extracted with 70% ethanol at 65°C four times for 30 min each with occasional vortexing, and then extracted sequentially with 100% ethanol, 100% methanol, and 100% acetone for 30 min each at room temperature on a rotator at 40 RPM and then dried. Samples were destarched with α-amylase from porcine pancreas (Sigma AS6255) in the tris-maleate buffer as previously described (Pettolino et al., 2012), precipitated with cold absolute ethanol and then washed four times with cold absolute ethanol. Destarched AIR samples were hydrolyzed with 2 M trifluoroacetic acid at 120°C for 90 min and the trifluoroacetic acid was evaporated under a stream of air. Monosaccharides were reduced with 0.5 ml of 20 mg/ml $NaBH_4$ in dimethyl sulfoxide (DMSO) with 0.1 ml of 1 M NH_4OH, neutralized with glacial acetic acid, and acetylated with 0.1 ml 1-methylimidazole and 0.75 ml anhydrous acetic anhydride. Derivatized monosaccharides were repeatedly partitioned between water and dichloromethane and then resuspended in dichloromethane. Derivatives were separated by gas chromatography on a Restek 10 120 RTX-1 column in an Agilent 6890 N/5973 GC–MS. Injection temperature was 100°C; temperature was increased to 170°C at 40°C min^{-1}, to 210°C at 5°C min^{-1}, to 300°C at 40°C min^{-1}, and then held at 300°C for 2 min. Helium flow was 1 ml min^{-1} and samples were injected with 1:10 split injection. Molar amounts of rhamnose, fucose, arabinose, xylose, mannose, glucose, and galactose were determined by comparison to known standards (Sigma) based on total ion counts for each elution peak. Glucose and galactose had identical retention times and so only the total combined amount of glucose and galactose was measured.

ACKNOWLEDGMENTS

We thank Mai Tran for assistance with polarized fluorescence microscopy and Chantal LeBlanc and Benoit Mermaz for assistance with flow cytometry. This research made use of the Chemical and Biophysical Instrumentation Center at Yale University.

FUNDING INFORMATION

This project was supported by grant MCB-1615387 from the National Science Foundation to V.F.I. FESEM and polarized light studies were supported in part by the Division of Chemical Sciences, Geosciences, and Biosciences, Office of Basic Energy Sciences of the U.S. Department of Energy (grant no. DE-FG-03ER15421 to T.I.B). This research was supported in part by competitive fellowship funds from the Laura and Arthur Colwin Fund of the Marine Biological Laboratory in Woods Hole, MA. R.O. acknowledges support from the National Institute of General Medical Sciences through grant numbers R01GM114274 and R35GM131843 and by the Inoué Endowment Fund of the Marine Biological Laboratory.

CONFLICT OF INTEREST

The authors declare no conflict of interest.

DATA AVAILABILITY STATEMENT

All relevant data can be found within the manuscript and its supporting materials.

SUPPORTING INFORMATION

Additional Supporting Information may be found in the online version of this article.

Figure S1. Macrofibrils are not sensitive to pectolyase digestion.

Stage 14 petals *rhm1-3* were cut to expose the interior of cells, digested with pectolyase, stained with fast scarlet, and then imaged with Airyscan confocal microscopy. Images are max-projections of Z-stacks with fast scarlet staining overlaid with DIC images. Yellow arrows denote largely intact cells with visible cellulose staining that have been cut open. (a) An *rhm1-3* petal not treated with pectolyase has many visible cellulose aggregations. (b) An *rhm1-3* petal digested with pectolyase has many visible cellulose aggregations. Bars = 5 μm.

Figure S2. Measurement of heterogeneity of cellulose distribution.

(a) Example images of a conical petal epidermal cell stained with fast scarlet and imaged with Airyscan confocal microscopy (left) and DIC (right). A line (yellow) was drawn on the cell parallel to the cuticular ridges and roughly perpendicular to the cellulose striations, and the heterogeneity of cellulose distribution was calculated as the standard deviation of intensity along that line divided by the mean intensity. Bar = 5 μm. (b) Plot of intensity versus position for the line shown in (a). The frequency of distinct cellulose striations was measured as the number of distinct peaks (red dots) along the line. (c) The mean ± standard deviation of the heterogeneity of cellulose distribution was measured for successive flowers in each inflorescence. Shading indicates the flower stage.

Figure S3. Cellulose aggregation correlates with abnormal cell morphology.

Stage 14 petals of the indicated genotypes were stained with fast scarlet and imaged with Airyscan confocal fluorescence microscopy. (a, b) Abaxial petal blade cells, (c, d) Adaxial petal claw cells, (e–g) Conical epidermal cells of the adaxial petal blade, (a′–g′) DIC images corresponding to (a–g), (h, i) Images of flowers show the twisted claws of the *spr2* mutant, (j, k) Adaxial petal claw cells, imaged as for a–g, (j′, k′) DIC images corresponding to j, k, (l) Diagram of petal regions. Bars = 1 mm in h, i and 5 μm in all other panels.

Figure S4. Cellulose orientation data.

Orientation of cellulose measured by polarized confocal microscopy of fast scarlet-stained conical petal epidermal cells. The same data are shown in Figure 5e, but each column is from a single petal each from a different plant, with the dots representing the values from individual cells.

Figure S5. Polyploidy increases petal cell expansion without altering monosaccharide composition.

(a) Representative images of wild-type and *rhm1* mutant flowers from diploid (2*n*), tetraploid (4*n*), or octoploid (8*n*) plants. Bar = 1 mm. (b) Representative profile images of conical petal epidermal cells taken from ~200 μm thick sections. Bar = 10 μm. (c) Cell wall composition of mixed-stage flowers evaluated as molar percentages of the indicated neutral monosaccharides. Levels of rhamnose (Rha), fucose (Fuc), arabinose (Ara), xylose (Xyl), and combined levels of galactose and glucose (Gal + Glc) were measured. Uronic acid levels were not assayed. Bars plot the mean ± standard deviation for three biological replicates per genotype. For each genotype, there were no statistically significant differences in the levels of any monosaccharide between diploid and tetraploid plants by *t*-test.

REFERENCES

Anderson, C.T., **Carroll, A.**, **Akhmetova, L.** & **Somerville, C.** (2010) Real-time imaging of cellulose reorientation during cell wall expansion in *Arabidopsis* roots. *Plant Physiology*, **152**, 787–796. Available from: https://doi.org/10.1104/pp.109.150128

Armezzani, A., **Abad, U.**, **Ali, O.**, **Andres Robin, A.**, **Vachez, L.**, **Larrieu, A.** ***et al.*** (2018) Transcriptional induction of cell wall remodelling genes is coupled to microtubule-driven growth isotropy at the shoot apex in *Arabidopsis*. *Development*, **145**. Available from: https://doi.org/10.1242/dev.162255

Atmodjo, M.A., **Hao, Z.** & **Mohnen, D.** (2013) Evolving views of pectin biosynthesis. *Annual Review of Plant Biology*, **64**, 747–779. Available from: https://doi.org/10.1146/annurev-arplant-042811-105534

Baskin, T.I. (2001) On the alignment of cellulose microfibrils by cortical microtubules: a review and a model. *Protoplasma*, **215**, 150–171. Available from: https://doi.org/10.1007/BF01280311

Baskin, T.I. (2005) Anisotropic expansion of the plant cell wall. *Annual Review of Cell and Developmental Biology*, **21**, 203–222. Available from: https://doi.org/10.1146/annurev.cellbio.20.082503.103053

Baskin, T.I., **Busby, C.H.**, **Fowke, L.C.**, **Sammut, M.** & **Gubler, F.** (1992) Improvements in immunostaining samples embedded in methacrylate: localization of microtubules and other antigens throughout developing organs in plants of diverse taxa. *Planta*, **187**, 405–413. Available from: https://doi.org/10.1007/BF00195665

Belli, S., **Dussi, S.**, **Dijkstra, M.** & **van Roij, R.** (2014) Density functional theory for chiral nematic liquid crystals. *Physical Review E*, **90**, 020503. Available from: https://doi.org/10.1103/PhysRevE.90.020503

Chakraborty, J., **Luo, J.** & **Dyson, R.J.** (2021) Lockhart with a twist: modelling cellulose microfibril deposition and reorientation reveals twisting plant cell growth mechanisms. *Journal of Theoretical Biology*, **525**, 110736. Available from: https://doi.org/10.1016/j.jtbi.2021.110736

Chan, J. & **Coen, E.** (2020) Interaction between autonomous and microtubule guidance systems controls cellulose synthase trajectories. *Current Biology*, **30**, 941–947.e2. Available from: https://doi.org/10.1016/j.cub.2019.12.066

Clough, S.J. & **Bent, A.F.** (1998) Floral dip: a simplified method for agrobacterium-mediated transformation of *Arabidopsis thaliana*. *The Plant Journal*, **16**, 735–743. Available from: https://doi.org/10.1385/1-59745-130-4:87

Cosgrove, D.J. (2018) Nanoscale structure, mechanics and growth of epidermal cell walls. *Current Opinion in Plant Biology*, **46**, 77–86. Available from: https://doi.org/10.1016/j.pbi.2018.07.016

Daher, F.B. & **Braybrook, S.A.** (2015) How to let go: pectin and plant cell adhesion. *Frontiers in Plant Science*, **6**, 523. Available from: https://doi.org/10.3389/fpls.2015.00523

Dick-Perez, M., **Zhang, Y.**, **Hayes, J.**, **Salazar, A.**, **Zabotina, O.A.** & **Hong, M.** (2011) Structure and interactions of plant cell-wall polysaccharides by two- and three-dimensional magic-angle-spinning solid-state NMR. *Biochemistry*, **50**, 989–1000. Available from: https://doi.org/10.1021/bi101795q

Diet, A., **Link, B.**, **Seifert, G.J.**, **Schellenberg, B.**, **Wagner, U.**, **Pauly, M.** ***et al.*** (2006) The *Arabidopsis* root hair cell wall formation mutant *lrx1* is suppressed by mutations in the *RHM1* gene encoding a UDP-L-rhamnose synthase. *Plant Cell*, **18**, 1630–1641. Available from: https://doi.org/10.1105/tpc.105.038653

Ding, S.-Y. & **Himmel, M.E.** (2006) The maize primary cell wall microfibril: a new model derived from direct visualization. *Journal of Agricultural and Food Chemistry*, **54**, 597–606. Available from: https://doi.org/10.1021/jf051851z

Donaldson, L. (2007) Cellulose microfibril aggregates and their size variation with cell wall type. *Wood Science and Technology*, **41**, 443–460. Available from: https://doi.org/10.1007/s00226-006-0121-6

Dong, J., **LeBlanc, C.**, **Poulet, A.**, **Mermaz, B.**, **Villarino, G.**, **Webb, K.M.** ***et al.*** (2021) H3.1K27me1 maintains transcriptional silencing and genome stability by preventing GCN5-mediated histone acetylation. *Plant Cell*, **33**, 961–979. Available from: https://doi.org/10.1093/plcell/koaa027

Du, J., **Kirui, A.**, **Huang, S.**, **Wang, L.**, **Barnes, W.J.**, **Kiemle, S.N.** ***et al.*** (2020) Mutations in the pectin methyltransferase QUASIMODO2 influence cellulose biosynthesis and wall integrity in *Arabidopsis*. *Plant Cell*, **32**, 3576–3597. Available from: https://doi.org/10.1105/tpc.20.00252

Ebert, B., **Birdseye, D.**, **Liwanag, A.J.M.**, **Laursen, T.**, **Rennie, E.A.**, **Guo, X.** ***et al.*** (2018) The three members of the *Arabidopsis* glycosyltransferase family 92 are functional β-1,4-galactan synthases. *Plant & Cell Physiology*, **59**, 2624–2636. Available from: https://doi.org/10.1093/pcp/pcy180

Emons, A.M.C., **Derksen, J.** & **Sassen, M.M.A.** (1992) Do microtubules orient plant cell wall microfibrils? *Physiologia Plantarum*, **84**, 486–493. Available from: https://doi.org/10.1111/j.1399-3054.1992.tb04695.x

Fan, Y., **Burkart, G.M.** & **Dixit, R.** (2018) The *Arabidopsis* SPIRAL2 protein targets and stabilizes microtubule minus ends. *Current Biology*, **28**, 987–994.e3. Available from: https://doi.org/10.1016/j.cub.2018.02.014

Ferreira, T., **Miura, K.**, **Chef, B.** & **Eglinger, J.** (2015) Scripts: BAR 1.1.6. Available from: https://doi.org/10.5281/zenodo.28838

Furutani, I., **Watanabe, Y.**, **Prieto, R.**, **Masukawa, M.**, **Suzuki, K.**, **Naoi, K.** ***et al.*** (2000) The SPIRAL genes are required for directional control of cell elongation in *Arabidopsis thaliana*. *Development*, **127**, 4443–4453. Available from: https://doi.org/10.1101/gad.866201

Hamant, O., **Heisler, M.G.**, **Jönsson, H.**, **Krupinski, P.**, **Uyttewaal, M.**, **Bokov, P.** ***et al.*** (2008) Developmental patterning by mechanical signals in *Arabidopsis*. *Science*, **322**, 1650–1655. Available from: https://doi.org/10.1126/science.1165594

Hanley, S.J., **Revol, J.-F.**, **Godbout, L.** & **Gray, D.G.** (1997) Atomic force microscopy and transmission electron microscopy of cellulose from *Micrasterias denticulata*; evidence for a chiral helical microfibril twist. *Cellulose*, **4**, 209–220. Available from: https://doi.org/10.1023/a:1018483722417

Huang, T. & **Irish, V.F.** (2015) Temporal control of plant organ growth by TCP transcription factors. *Current Biology*, **25**, 1765–1770. Available from: https://doi.org/10.1016/j.cub.2015.05.024

Irish, V.F. (2008) The *Arabidopsis* petal: a model for plant organogenesis. *Trends in Plant Science*, **13**, 430–436. Available from: https://doi.org/10.1016/j.tplants.2008.05.006

Ishida, T., **Kaneko, Y.**, **Iwano, M.** & **Hashimoto, T.** (2007) Helical microtubule arrays in a collection of twisting tubulin mutants of *Arabidopsis thaliana*. *Proceedings of the National Academy of Sciences of the United States of America*, **104**, 8544–8549. Available from: https://doi.org/10.1073/pnas.0701224104

Jensen, J.K., **Sorensen, S.O.**, **Harholt, J.**, **Geshi, N.**, **Sakuragi, Y.**, **Moller, I.** ***et al.*** (2008) Identification of a xylogalacturonan xylosyltransferase involved in pectin biosynthesis in *Arabidopsis*. *Plant Cell*, **20**, 1289–1302. Available from: https://doi.org/10.1105/tpc.107.050906

Jones, P., **Messner, B.**, **Nakajima, J.-I.**, **Schäffner, A.R.** & **Saito, K.** (2003) UGT73C6 and UGT78D1, glycosyltransferases involved in Flavonol glycoside biosynthesis in *Arabidopsis thaliana*. *The Journal of Biological Chemistry*, **278**, 43910–43918. Available from: https://doi.org/10.1074/jbc.M303523200

Kay, Q.O.N., **Daoud, H.S.** & **Stirton, C.H.** (1981) Pigment distribution, light reflection and cell structure in petals. *Botanical Journal of the Linnean Society*, **83**, 57–83. Available from: https://doi.org/10.1111/j.1095-8339.1981.tb00129.x

Liang, B.M., **Dennings, A.M.**, **Sharp, R.E.** & **Baskin, T.I.** (1996) Consistent handedness of microtubule helical arrays in maize and *Arabidopsis* primary roots. *Protoplasma*, **190**, 8–15. Available from: https://doi.org/10.1007/BF01281190

Lin, D., **Lopez-Sanchez, P.** & **Gidley, M.J.** (2016) Interactions of pectins with cellulose during its synthesis in the absence of calcium. *Food Hydrocolloids*, **52**, 57–68. Available from: https://doi.org/10.1016/j.foodhyd.2015.06.004

Lyczakowski, J.J., **Bourdon, M.**, **Terrett, O.M.**, **Helariutta, Y.**, **Wightman, R.** & **Dupree, P.** (2019) Structural imaging of native cryo-preserved secondary cell walls reveals the presence of macrofibrils and their formation requires normal cellulose, lignin and xylan biosynthesis. *Frontiers in Plant Science*, **10**, 1398. Available from: https://doi.org/10.3389/fpls.2019.01398

Majoinen, J., **Kontturi, E.**, **Ikkala, O.** & **Gray, D.G.** (2012) SEM imaging of chiral nematic films cast from cellulose nanocrystal suspensions. *Cellulose*, **19**, 1599–1605. Available from: https://doi.org/10.1007/s10570-012-9733-1

Marga, F., **Grandbois, M.**, **Cosgrove, D.J.** & **Baskin, T.I.** (2005) Cell wall extension results in the coordinate separation of parallel microfibrils: evidence from scanning electron microscopy and atomic force microscopy. *The Plant Journal*, **43**, 181–190. Available from: https://doi.org/10.1111/j.1365-313X.2005.02447.x

Matthews, J.F., **Skopec, C.E.**, **Mason, P.E.**, **Zuccato, P.**, **Torget, R.W.**, **Sugiyama, J.** ***et al.*** (2006) Computer simulation studies of microcrystalline cellulose Iβ. *Carbohydrate Research*, **341**, 138–152. Available from: https://doi.org/10.1016/j.carres.2005.09.028

Morrow, S.M., **Bissette, A.J.** & **Fletcher, S.P.** (2017) Transmission of chirality through space and across length scales. *Nature Nanotechnology*, **12**, 410–419. Available from: https://doi.org/10.1038/nnano.2017.62

Mouille, G., **Ralet, M.-C.**, **Cavelier, C.**, **Eland, C.**, **Effroy, D.**, **Hématy, K.** ***et al.*** (2007) Homogalacturonan synthesis in *Arabidopsis thaliana* requires a Golgi-localized protein with a putative methyltransferase domain. *The Plant Journal*, **50**, 605–614. Available from: https://doi.org/10.1111/j.1365-313X.2007.03086.x

Ndeh, D., **Rogowski, A.**, **Cartmell, A.**, **Luis, A.S.**, **Baslé, A.**, **Gray, J.** ***et al.*** (2017) Complex pectin metabolism by gut bacteria reveals novel catalytic functions. *Nature*, **544**, 65–70. Available from: https://doi.org/10.1038/nature21725

Oka, T., **Nemoto, T.** & **Jigami, Y.** (2007) Functional analysis of *Arabidopsis thaliana* RHM2/MUM4, a multidomain protein involved in UDP-D-glucose to UDP-L-rhamnose conversion. *The Journal of Biological Chemistry*, **282**, 5389–5403. Available from: https://doi.org/10.1074/jbc.M610196200

Oldenbourg, R. & **Mei, G.** (1995) New polarized light microscope with precision universal compensator. *Journal of Microscopy*, **180**, 140–147. Available from: https://doi.org/10.1111/j.1365-2818.1995.tb03669.x

O'Neill, M.A., **Eberhard, S.**, **Albersheim, P.** & **Darvill, A.G.** (2001) Requirement of borate cross-linking of cell wall rhamnogalacturonan II for *Arabidopsis* growth. *Science*, **294**, 846–849. Available from: https://doi.org/10.1126/science.1062319

Paavilainen, S., **Róg, T.** & **Vattulainen, I.** (2011) Analysis of twisting of cellulose nanofibrils in atomistic molecular dynamics simulations. *The Journal of Physical Chemistry. B*, **115**, 3747–3755. Available from: https://doi.org/10.1021/jp111459b

Pabst, M., **Fischl, R.M.**, **Brecker, L.**, **Morelle, W.**, **Fauland, A.**, **Köfeler, H.** ***et al.*** (2013) Rhamnogalacturonan II structure shows variation in the side chains monosaccharide composition and methylation status within and across different plant species. *The Plant Journal*, **76**, 61–72. Available from: https://doi.org/10.1111/tpj.12271

Pettolino, F.A., **Walsh, C.**, **Fincher, G.B.** & **Bacic, A.** (2012) Determining the polysaccharide composition of plant cell walls. *Nature Protocols*, **7**, 1590–1607. Available from: https://doi.org/10.1038/nprot.2012.081

Polko, J.K. & **Kieber, J.J.** (2019) The regulation of cellulose biosynthesis in plants. *Plant Cell*, **31**, 282–296. Available from: https://doi.org/10.1105/tpc.18.00760

Probine, M.C. (1963) Cell growth and the structure and mechanical properties of the wall in internodal cells of *Nitella opaca*: III. Spiral growth and cell wall structure. *Journal of Experimental Botany*, **14**, 101–113.

Reiter, W.D., **Chapple, C.C.** & **Somerville, C.R.** (1993) Altered growth and cell walls in a fucose-deficient mutant of *Arabidopsis*. *Science*, **261**, 1032–1035. Available from: https://doi.org/10.1126/science.261.5124.1032

Reiter, W.D. & **Vanzin, G.F.** (2001) Molecular genetics of nucleotide sugar interconversion pathways in plants. *Plant Molecular Biology*, **47**, 95–113.

Ren, H., **Dang, X.**, **Cai, X.**, **Yu, P.**, **Li, Y.**, **Zhang, S.** ***et al.*** (2017) Spatiotemporal orientation of microtubules controls conical cell shape in *Arabidopsis thaliana* petals. *PLoS Genetics*, **13**, e1006851. Available from: https://doi.org/10.1371/journal.pgen.1006851

Revol, J.F., **Bradford, H.**, **Giasson, J.**, **Marchessault, R.H.** & **Gray, D.G.** (1992) Helicoidal self-ordering of cellulose microfibrils in aqueous suspension. *International Journal of Biological Macromolecules*, **14**, 170–172. Available from: https://doi.org/10.1016/S0141-8130(05)80008-X

Roelofsen, P.A. (1966) Ultrastructure of the wall in growing cells and its relation to the direction of the growth. *Advances in Botanical Research*, **2**, 69–149. Available from: https://doi.org/10.1016/S0065-2296(08)60250-5

Rongpipi, S., **Ye, D.**, **Gomez, E.D.** & **Gomez, E.W.** (2018) Progress and opportunities in the characterization of cellulose – an important regulator of cell wall growth and mechanics. *Frontiers in Plant Science*, **9**, 1894. Available from: https://doi.org/10.3389/fpls.2018.01894

Ryden, P., **Sugimoto-Shirasu, K.**, **Smith, A.C.**, **Findlay, K.**, **Reiter, W.-D.** & **McCann, M.C.** (2003) Tensile properties of *Arabidopsis* cell walls depend on both a xyloglucan cross-linked microfibrillar network and rhamnogalacturonan II-borate complexes. *Plant Physiology*, **132**, 1033–1040. Available from: https://doi.org/10.1104/pp.103.021873

Saffer, A.M. (2018) Expanding roles for pectins in plant development. *Journal of Integrative Plant Biology*, **60**, 910–923. Available from: https://doi.org/10.1111/jipb.12662

Saffer, A.M., **Carpita, N.C.** & **Irish, V.F.** (2017) Rhamnose-containing cell wall polymers suppress helical plant growth independently of microtubule orientation. *Current Biology*, **27**, 2248–2259.e4. Available from: https://doi.org/10.1016/j.cub.2017.06.032

Saffer, A.M. & **Irish, V.F.** (2017) Isolation of mutants with abnormal petal epidermal cell morphology. *Plant Signaling & Behavior*, **12**, e1382794. Available from: https://doi.org/10.1080/15592324.2017.1382794

Saffer, A.M. & **Irish, V.F.** (2018) Flavonol rhamnosylation indirectly modifies the cell wall defects of *RHAMNOSE BIOSYNTHESIS1* mutants by altering rhamnose flux. *The Plant Journal*, **94**, 649–660. Available from: https://doi.org/10.1111/tpj.13885

Schindelin, J., **Arganda-Carreras, I.**, **Frise, E.**, **Kaynig, V.**, **Longair, M.**, **Pietzsch, T.** ***et al.*** (2012) Fiji: an open-source platform for biological-image analysis. *Nature Publishing Group*, **9**, 676–682. Available from: https://doi.org/10.1038/nmeth.2019

Schütz, C., **Agthe, M.**, **Fall, A.B.**, **Gordeyeva, K.**, **Guccini, V.**, **Salajková, M.** ***et al.*** (2015) Rod packing in chiral nematic cellulose nanocrystal dispersions studied by small-angle X-ray scattering and laser diffraction. *Langmuir*, **31**, 6507–6513. Available from: https://doi.org/10.1021/acs.langmuir.5b00924

Sedbrook, J.C. (2002) The *Arabidopsis* SKU5 gene encodes an extracellular glycosyl phosphatidylinositol-anchored glycoprotein involved in directional root growth. *Plant Cell*, **14**, 1635–1648. Available from: https://doi.org/10.1105/tpc.002360

Sellen, D.B. (1983) The response of mechanically anisotropic cylindrical cells to multiaxial stress. *Journal of Experimental Botany*, **34**, 681–687. Available from: https://doi.org/10.1093/jxb/34.6.681

Smyth, D.R. (2016) Helical growth in plant organs: mechanisms and significance. *Development*, **143**, 3272–3282. Available from: https://doi.org/10.1242/dev.134064

Smyth, D.R., **Bowman, J.L.** & **Meyerowitz, E.M.** (1990) Early flower development in *Arabidopsis*. *Plant Cell*, **2**, 755–767. Available from: https://doi.org/10.1105/tpc.2.8.755

Spira, F., **Cuylen-Haering, S.**, **Mehta, S.**, **Samwer, M.**, **Reversat, A.**, **Verma, A.** ***et al.*** (2017) Cytokinesis in vertebrate cells initiates by contraction of an equatorial actomyosin network composed of randomly oriented filaments. *eLife*, **6**, e30867. Available from: https://doi.org/10.7554/eLife.30867

Sugimoto, K., **Williamson, R.E.** & **Wasteneys, G.O.** (2000) New techniques enable comparative analysis of microtubule orientation, wall texture, and growth rate in intact roots of *Arabidopsis*. *Plant Physiology*, **124**, 1493–1506. Available from: https://doi.org/10.1104/pp.124.4.1493

Thimm, J.C., **Burritt, D.J.**, **Ducker, W.A.** & **Melton, L.D.** (2009) Pectins influence microfibril aggregation in celery cell walls: an atomic force microscopy study. *Journal of Structural Biology*, **168**, 337–344. Available from: https://doi.org/10.1016/j.jsb.2009.06.017

Thomas, J., **Idris, N.A.** & **Collings, D.A.** (2017) Pontamine fast scarlet 4B bifluorescence and measurements of cellulose microfibril angles. *Journal of Microscopy*, **268**, 13–27. Available from: https://doi.org/10.1111/jmi.12582

Updegraff, D.M. (1969) Semimicro determination of cellulose in biological materials. *Analytical Biochemistry*, **32**, 420–424.

Usov, I., **Nyström, G.**, **Adamcik, J.**, **Handschin, S.**, **Schütz, C.**, **Fall, A.** ***et al.*** (2015) Understanding nanocellulose chirality and structure–properties relationship at the single fibril level. *Nature Communications*, **6**, 7564. Available from: https://doi.org/10.1038/ncomms8564

Verger, S., **Liu, M.** & **Hamant, O.** (2019) Mechanical conflicts in twisting growth revealed by cell-cell adhesion defects. *Frontiers in Plant Science*, **10**, 173. Available from: https://doi.org/10.3389/fpls.2019.00173

Wada, H. & **Matsumoto, D.** (2018) Twisting growth in plant roots. In: *Plant Biomechanics*. Cham: Springer International Publishing, pp. 127–140. Available from: https://doi.org/10.1007/978-3-319-79099-2_6

Wang, T., **Park, Y.B.**, **Cosgrove, D.J.** & **Hong, M.** (2015) Cellulose-pectin spatial contacts are inherent to never-dried *Arabidopsis* primary cell walls: evidence from solid-state nuclear magnetic resonance. *Plant Physiology*, **168**, 871–884. Available from: https://doi.org/10.1104/pp.15.00665

Wang, T., **Zabotina, O.** & **Hong, M.** (2012) Pectin–cellulose interactions in the *Arabidopsis* primary cell wall from two-dimensional magic-angle-spinning solid-state nuclear magnetic resonance. *Biochemistry*, **51**, 9846–9856. Available from: https://doi.org/10.1021/bi3015532

Whitney, H.M., **Bennett, K.M.V.**, **Dorling, M.**, **Sandbach, L.**, **Prince, D.**, **Chittka, L.** ***et al.*** (2011) Why do so many petals have conical epidermal cells? *Annals of Botany*, **108**, 609–616. Available from: https://doi.org/10.1093/aob/mcr065

Wu, X. & **Hammer, J.A.** (2021) ZEISS Airyscan: Optimizing Usage for Fast, Gentle, Super-Resolution Imaging. In: Brzostowski, J. & Sohn, H. (Eds.) *Confocal Microscopy, Methods in Molecular Biology*. New York, NY, USA: Springer, pp. 111–130. Available from: https://doi.org/10.1007/978-1-0716-1402-0_5

Yang, Y., **Chen, B.**, **Dang, X.**, **Zhu, L.**, **Rao, J.**, **Ren, H.** ***et al.*** (2019) *Arabidopsis* IPGA1 is a microtubule-associated protein essential for cell expansion during petal morphogenesis. *Journal of Experimental Botany*, **70**, 5231–5243. Available from: https://doi.org/10.1093/jxb/erz284

Yoneda, A., **Ito, T.**, **Higaki, T.**, **Kutsuna, N.**, **Saito, T.**, **Ishimizu, T.** ***et al.*** (2010) Cobtorin target analysis reveals that pectin functions in the deposition of cellulose microfibrils in parallel with cortical microtubules. *The Plant Journal*, **64**, 657–667. Available from: https://doi.org/10.1111/j.1365-313X.2010.04356.x

Yonekura-Sakakibara, K., **Tohge, T.**, **Matsuda, F.**, **Nakabayashi, R.**, **Takayama, H.**, **Niida, R.** ***et al.*** (2008) Comprehensive flavonol profiling and transcriptome coexpression analysis leading to decoding gene-metabolite correlations in *Arabidopsis*. *Plant Cell*, **20**, 2160–2176. Available from: https://doi.org/10.1105/tpc.108.058040

Yonekura-Sakakibara, K., **Tohge, T.**, **Niida, R.** & **Saito, K.** (2007) Identification of a flavonol 7- O-rhamnosyltransferase gene determining flavonoid pattern in *Arabidopsis* by transcriptome coexpression analysis and reverse genetics. *The Journal of Biological Chemistry*, **282**, 14932–14941. Available from: https://doi.org/10.1074/jbc.M611498200

Zhang, T., **Zheng, Y.** & **Cosgrove, D.J.** (2016) Spatial organization of cellulose microfibrils and matrix polysaccharides in primary plant cell walls as imaged by multichannel atomic force microscopy. *The Plant Journal*, **85**, 179–192. Available from: https://doi.org/10.1111/tpj.13102

Zhang, Y., **Yu, J.**, **Wang, X.**, **Durachko, D.M.**, **Zhang, S.** & **Cosgrove, D.J.** (2021) Molecular insights into the complex mechanics of plant epidermal cell walls. *Science*, **372**, 706–711. Available from: https://doi.org/10.1126/science.abf2824

Zykwinska, A., **Thibault, J.F.** & **Ralet, M.C.** (2007) Organization of pectic arabinan and galactan side chains in association with cellulose microfibrils in primary cell walls and related models envisaged. *Journal of Experimental Botany*, **58**, 1795–1802. Available from: https://doi.org/10.1093/jxb/erm037

Zykwinska, A.W., **Ralet, M.-C.J.**, **Garnier, C.D.** & **Thibault, J.-F.J.** (2005) Evidence for in vitro binding of pectin side chains to cellulose. *Plant Physiology*, **139**, 397–407. Available from: https://doi.org/10.1104/pp.105.065912